Mon. Not. R. Astron. Soc. **000**, 1–8 (2002) Printed 3 June 2005 (MN LATEX style file v1.4)

The 2000 Periastron Passage of PSR B1259–63

T. W. Connors[1⋆], S. Johnston[1], R. N. Manchester[2] and D. McConnell[2]
[1] *School of Physics, University of Sydney, NSW 2006, Australia*
[2] *Australia Telescope National Facility, CSIRO, PO Box 1710, Epping NSW 2121, Australia*

3 June 2005

ABSTRACT
We report here on a sequence of 28 observations of the binary pulsar system PSR B1259−63/SS2883 at four radio frequencies made with the Australia Telescope Compact Array around the time of the 2000 periastron passage. Observations made on 2000 Sep 1 show that the pulsar's apparent rotation measure (RM) reached a maximum of -14800 ± 1800 rad m^{-2}, some 700 times the value measured away from periastron, and is the largest astrophysical RM measured. This value, combined with the dispersion measure implies a magnetic field in the Be star's wind of 6 mG. We find that the light curve of the unpulsed emission is similar to that obtained during the 1997 periastron but that differences in detail imply that the emission disc of the Be star is thicker and/or of higher density. The behaviour of the light curve at late times is best modelled by the adiabatic expansion of a synchrotron bubble formed in the pulsar/disc interaction. The expansion rate of the bubble ∼12 km s^{-1} is surprisingly low but the derived magnetic field of 1.6 G close to that expected.

Key words: radiation mechanisms: non-thermal — binaries: close — stars: emission-line, Be — stars: individual: SS2883 — pulsars: individual: PSR B1259−63 — radio continuum: stars.

1 INTRODUCTION

PSR B1259−63 was discovered in 1990 in a survey of the Galactic plane for pulsars (Johnston et al. 1992a) and was subsequently found to be in a 3.4-yr, highly eccentric orbit about a ∼10 M$_\odot$ Be star, SS2883 (Johnston et al. 1992b). It remains the only known radio pulsar with a Be star companion. The pulsar has a spin period of ∼48 ms, a characteristic age of 0.33 Myr, and a moderate magnetic field of 3.3×10^{11} G. The dispersion measure (DM) of 146.7 cm^{-3}pc yields a distance of 4.5 kpc in the model of Taylor & Cordes (1993), however scintillation (McClure-Griffiths et al. 1997) and optical (Johnston et al. 1994) measurements indicate a distance closer to 1.5 kpc. The pulse profile, shown in Figure 1, has two almost equal intensity peaks both of which are highly (and almost orthogonally) polarised, with an average interstellar rotation measure (RM) measured away from periastron of +21 rad m^{-2} (Manchester & Johnston 1995).

Optical observations (Johnston et al. 1994) show that SS2883 is of spectral type B2e, and thus has a mass of ∼10 M$_\odot$ and a radius R$_c$ ∼6 R$_\odot$. Assuming a pulsar mass of 1.4 M$_\odot$, the implied inclination angle of the binary orbit to the plane of the sky is 36°. The Hα emission line shows that the Be star's emission disc extends to at least 20 R$_c$, just inside the pulsar's orbital radius at periastron. Timing measurements have shown that the disc of the Be star is likely to be highly inclined with respect to the orbital plane (Wex et al. 1998).

The 1997 periastron was observed extensively by John-

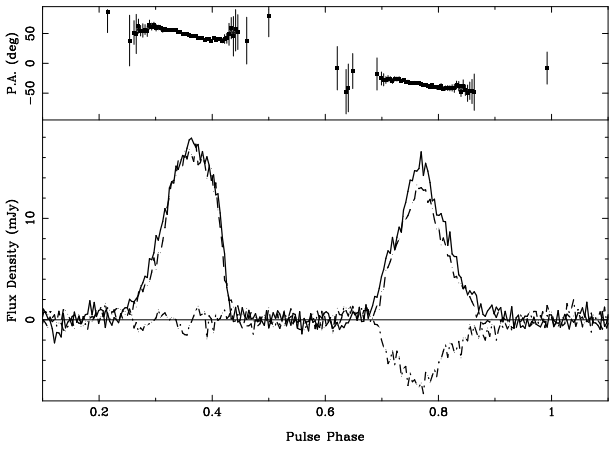

Figure 1. Mean pulse profile at 1.4 GHz. Position angle is shown on top, and the total intensity (solid line), linear (dashed line) and circular (dash-dot line) polarisations are shown in the bottom panel.

⋆ Present address: Swinburne Centre for Astrophysics and Supercomputing, Swinburne University of Technology, Hawthorn, Vic 3122, Australia

ston et al. (1999, 2001) and a model for the transient emission was proposed by Ball et al. (1999) following earlier work by Melatos et al. (1995). In brief, unpulsed emission began at $\mathcal{T}-22$ and lasted until at least $\mathcal{T}+100$ (where $\mathcal{T}$ denotes the epoch of periastron). The spectral index of the unpulsed emission was in the range -0.5 to -0.7, a value indicative of synchrotron radiation. Peaks in the light curve at $\mathcal{T}-10$ and $\mathcal{T}+20$ coincide with the pulsar crossing through the emission disc of the Be star. The model therefore proposed that the synchrotron emission was generated in the shock between the relativistic pulsar wind and the outflowing disc of the Be star. Synchrotron losses, set by the magnetic field strength, then determined the decay time of the light curve. The decay time of the emission from the post-periastron disc crossing was substantially shorter than that of the pre-periastron decay.

The model predicted a frequency dependence for the end of the transient phase and verification of this late-time behaviour was a motivation for the 2000 periastron observations. Also, the improvements in the correlator and the data reduction software meant that the pulsar rotation measure (RM) and dispersion measure (DM) could be accurately obtained during this periastron passage. We therefore obtained data over 28 epochs from $\mathcal{T}-46$ to $\mathcal{T}+113$ during the 2000 periastron encounter. In section 2, we describe the observations. In section 3 we detail the results obtained and discuss their implications in section 4.

2 OBSERVATIONS

Observations were made at the Australia Telescope Compact Array (ATCA). The ATCA is an east-west synthesis telescope located near Narrabri, NSW and consists of six 22-m antennas on a 6 km track. On the ATCA, observations can be made simultaneously at either 1.4 and 2.4 GHz or 4.8 and 8.4 GHz with a bandwidth of 128 MHz at each frequency subdivided into 32 spectral channels, and full Stokes parameters. The ATCA is also capable of splitting each correlator cycle into bins corresponding to different phases of a pulsar's period, and in our case the pulse period of ∼48 ms was split into 16 bins.

A total of 28 observations between $\mathcal{T}-46$ and $\mathcal{T}+113$ were made using various ATCA configurations. Table 1 lists the relevant details. One of the ATCA primary flux calibrators, B0823−500 (flux densities of 5.5, 5.6, 3.1 and 1.4 Jy at 1.4, 2.5, 4.8 and 8.4 GHz respectively) or B1934−638 (14.9, 11.6, 5.8 and 2.8 Jy), was observed once during each session for ∼5 min. Each pair of bands was switched every ∼20 min, with an observation of the secondary phase calibrator (B1251−713; flux density ∼1 Jy at all frequencies) for ∼3 min leading each integration.

Data reduction and analysis were carried out with the MIRIAD package (Sault & Killeen 1998) using standard techniques. After flagging bad data, the primary calibrator was used for flux density and bandpass calibration and the secondary calibrator was used to solve for antenna gains, phases and polarisation leakage terms. The short baselines in the 750C array typically were completely flagged out at the two lower frequencies, because of excessive interference. After calibration, the data consist of 13 independent frequency channels each 8 MHz wide for each of the 16 phase bins.

Start time (UT)			Length	Array
yr	mon	day	(hr)	config
2000	Sep	01.00	4	6A
2000	Sep	15.05	4	6A
2000	Sep	23.05	4	6A
2000	Sep	25.05	4	6A
2000	Sep	27.06	4	6A
2000	Sep	29.00	4	6A
2000	Sep	30.88	4	6A
2000	Oct	02.74	4	6A
2000	Oct	05.22	4	6A
2000	Oct	06.88	4	6A
2000	Oct	11.05	4	6A
2000	Oct	14.79	4	6A
2000	Oct	18.89	4	6C
2000	Oct	23.01	4	6C
2000	Oct	26.97	4	6C
2000	Oct	30.71	4	6C
2000	Nov	04.85	8	6C
2000	Nov	07.79	2	6C
2000	Nov	10.84	4	6C
2000	Nov	15.93	4	1.5B
2000	Nov	20.72	4	1.5B
2000	Nov	26.72	4	1.5B
2000	Dec	08.84	4	1.5B
2000	Dec	11.72	4	1.5B
2000	Dec	19.86	4	1.5C
2000	Dec	26.79	5	750C
2001	Jan	08.49	5.5	750C
2001	Feb	07.72	4	6C

Table 1. Date, length of observation in hours, and array configuration for all observations of PSR B1259−63/SS2883 during the 2000 periastron passage. On Nov 7, only 1.4 and 2.4 GHz observations were made. On Dec 8 time-binning operation was not functional. Periastron occurred on Oct 17.3.

2.1 Total Flux Density

To measure the total flux density from the system (i.e. the pulsar plus any unpulsed emission) we first collapsed the 16 phase bins into one. Standard techniques of image inversion, cleaning and restoring were then performed. The flux density and associated errors were measured directly from the image with the routine IMFIT with the source assumed to be a point source at a fixed position given by the timing data (Wex et al. 1998).

2.2 Pulsar Flux Density

The UV binned data were first corrected for dispersion with the routine PSRFIX. We assume a constant DM of 146.7 $\mathrm{cm}^{-3}\mathrm{pc}$ for all the observations. Although the DM is known to vary close to periastron, our time resolution of only 3 ms made the increased time delay largely irrelevant. We then examined the pulse profile using and selected those bins which formed the off-pulse portion of the profile. The mean of the selected baseline bins is then subtracted from all the phase bins for every frequency channel and for each Stokes parameter using PSRBL. This has the effect of removing all sources from the image apart from the pulsar. The flux density of the pulsar was then obtained directly from the visibility data (with UVFLUX) without the need for further imaging. This process is valid in the absence of

Date	Day ($+\mathcal{T}$)	Observing Frequency 1384 MHz Pulsar (mJy)	1384 MHz Total (mJy)	2496 MHz Pulsar (mJy)	2496 MHz Total (mJy)	4800 MHz Pulsar (mJy)	4800 MHz Total (mJy)	8400 MHz Pulsar (mJy)	8400 MHz Total (mJy)
Sep 01	−46.4	5.36±0.12	8.00±0.73	4.77±0.19	4.61±0.20	2.75±0.10	2.76±0.18	1.76±0.08	1.81±0.16
Sep 15	−32.4	—	3.93±0.65	2.47±0.21	5.00±0.43	2.27±**1.28**	2.22±0.48	0.61±**0.61**	0.78±0.32
Sep 23	−24.4	—	1.64±0.37	—	3.34±0.33	2.15±0.17	2.28±0.39	0.61±0.09	0.64±0.19
Sep 25	−22.4	—	3.78±0.56	1.38±0.20	4.29±0.43	1.70±**0.61**	1.70±0.30	1.10±**0.67**	1.13±0.31
Sep 27	−20.4	—	2.03±0.29	—	1.62±0.25	0.60±0.10	1.43±0.34	0.44±0.09	0.65±0.25
Sep 29	−18.4	0.29±0.13	4.73±0.64	—	5.36±0.34	0.57±0.14	3.26±0.40	0.22±0.09	1.58±0.40
Sep 30	−16.5	—	6.44±1.06	—	6.86±0.31	—	4.62±0.38	—	2.86±0.42
Oct 02	−14.7	—	17.60±1.91	—	13.28±1.29	—	9.17±2.41	—	3.18±1.85
Oct 05	−12.2	—	27.39±2.62	—	23.27±1.57	—	12.06±3.71	—	3.09±2.20
Oct 06	−10.5	—	33.37±1.68	—	29.61±0.78	—	21.95±1.16	—	13.68±1.11
Oct 11	−6.4	—	39.64±2.91	—	29.83±2.01	—	13.93±3.33	—	3.27±2.05
Oct 14	−2.6	—	29.16±1.70	—	23.70±0.84	—	16.17±1.97	—	9.18±1.98
Oct 18	1.5	—	21.50±1.59	—	17.36±0.54	—	11.75±0.99	—	7.85±0.99
Oct 23	5.6	—	21.72±1.24	—	16.93±1.07	—	10.15±2.52	—	3.70±2.21
Oct 26	9.6	—	22.57±1.62	—	15.88±1.19	—	6.79±1.54	—	1.22±0.50
Oct 30	13.3	—	22.55±2.17	—	17.50±1.07	—	12.35±1.39	—	6.13±1.59
Nov 04	18.5	—	29.88±1.46	—	23.22±0.92	0.39±0.06	11.02±1.42	0.36±0.05	2.46±0.76
Nov 07	21.3	1.64±0.12	35.66±2.54	3.31±0.21	34.65±1.32				
Nov 10	24.4	2.97±0.17	36.95±2.27	5.12±**1.03**	34.60±1.46	4.33±0.18	22.95±2.01	1.59±**0.58**	13.40±1.55
Nov 15	29.5	3.75±0.18	32.04±3.15	3.08±0.12	24.62±1.15	1.89±**0.27**	13.81±1.86	1.48±0.13	7.06±1.72
Nov 20	34.3	3.33±0.13	26.69±2.70	3.61±0.17	23.61±0.80	2.94±0.09	17.27±1.06	0.86±0.08	9.62±0.99
Nov 26	40.3	3.69±0.11	20.73±1.73	3.83±0.17	18.92±0.64	1.63±0.08	11.06±0.77	1.60±**0.45**	6.88±0.85
Dec 08	52.3		18.47±2.28		13.36±0.72		7.83±0.77		4.02±0.73
Dec 11	55.3	4.05±0.15	15.47±1.72	3.56±0.19	11.70±0.38	1.11±0.12	5.43±0.32	1.65±0.10	3.80±0.33
Dec 19	63.4	4.41±0.20	15.58±1.62	3.64±0.20	10.30±0.71	2.38±**0.49**	5.07±1.35	0.57±**0.27**	1.39±0.61
Dec 26	70.4	5.09±0.18	10.25±1.84	4.11±0.12	7.47±0.55	1.92±0.08	5.19±0.55	1.07±0.06	0.75±0.41
Jan 08	83.1	5.28±**1.14**	13.52±3.46	4.76±**0.84**	10.38±0.60	1.85±0.09	5.09±0.41	0.48±0.06	2.56±0.38
Feb 07	113.3	3.60±**0.99**	10.85±0.86	3.39±**1.24**	7.97±0.63	3.87±**2.94**	6.46±2.08	0.74±**1.35**	2.19±1.31

Table 2. Flux densities for pulsed emission and total emission (pulsed plus unpulsed) for all 29 observations with the ATCA. Flux densities and errors for continuum and pulsar are from IMFIT. Flux densities and errors for pulsar only are from UVFLUX. Pulsar flux densities are omitted when no significant pulses could be seen.

sidelobes from any other source in the primary beam. The main source of error in this technique is determining which phase bins are off-pulse. This is especially true when the pulsar is weak and/or scattered. Generally we found that the error in the flux density given by the imaginary component in UVFLUX was equivalent to the value expected from thermal system noise considerations. Occasionally, a significantly larger measurement error was determined (indicated with bold type in Table 2) which was dominated by phase calibration errors.

2.3 Dispersion Measure

Even with our relatively crude time resolution of ∼3 ms per bin we are able to measure the DM across the band at 1.4 GHz with reasonable accuracy. To achieve this we determined the centroid of each of the two pulse components for each of the 13 frequency channels. The time delay in seconds for a given channel, c, relative to the first channel is given by (see e.g. Manchester & Taylor 1977)

$$t_c \;=\; 4149.94 \;\mathrm{DM}\; \left(\frac{1}{\nu_c^2} - \frac{1}{\nu_1^2}\right) \qquad (1)$$

where ν is the frequency of the channel in MHz. The DM can therefore be obtained by a straight-line fit to a plot of dispersion delay versus wavelength squared. The error bar on the DM is about one order of magnitude higher than from 'conventional' pulsar timing (Johnston et al. 2001).

2.4 Circular Polarisation

As the natural modes of the wind of the Be star and the interstellar plasma are circular, circularly polarised flux is not affected by propagation. We therefore used the measurement of the circular polarisation under each pulse component independently to verify our polarisation calibration. As before, the flux in Stokes V for two separate phase bin ranges corresponding to the two pulsar components was obtained from the visibility data via UVFLUX.

2.5 Linear Polarisation and RM

UVFLUX was used to measure Stokes Q and U in each channel for each phase bin and/or combinations of channels and phase bins. In practice, in order to boost signal to noise, we combine the phase bins together which correspond to each pulse component as Stokes Q and U do not vary rapidly through the pulse (see Fig 1). The position angle, ϕ_λ, of each pulse component at a given observing wavelength, λ, can be then be computed through

$$\phi_\lambda = 0.5 \times \tan^{-1}(U_\lambda/Q_\lambda). \qquad (2)$$

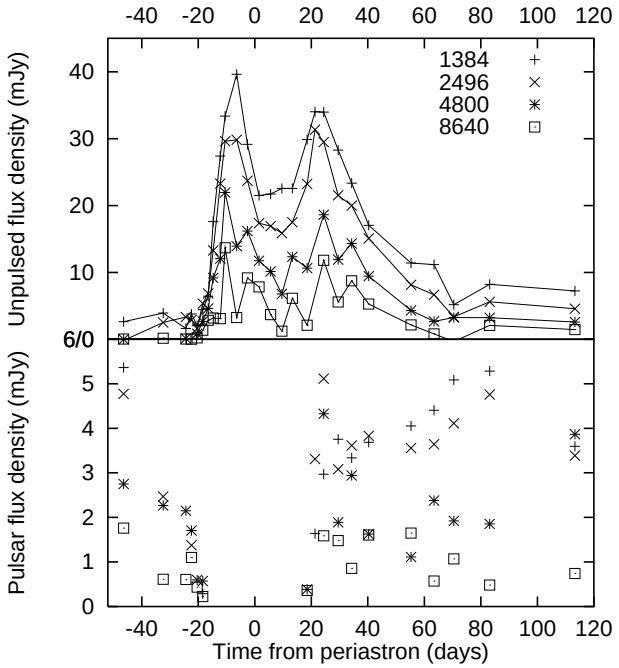

Figure 2. Light curves for the unpulsed emission (top) and the pulsar (bottom) from the 2000 periastron data. For clarity the error bars have been omitted.

The error on the position angle is given by

$$\Delta\phi = 0.5\epsilon/\sqrt{Q^2+U^2} \quad (3)$$

when both the Q and U measurements have the same rms error ϵ. Note that as the linear polarisation has a positive definite bias, this must be subtracted before the error is computed. The position angle is related to the RM by

$$\phi_\nu = \mathrm{RM}\,\lambda^2 \quad (4)$$

Hence, plotting position angle against λ^2 should yield a straight line with slope RM. This procedure was carried out for each of the two components independently.

3 RESULTS

The flux densities and their associated errors from the observations listed in Table 1 are given in Table 2. The table first lists the date of the observation, followed by the time from periastron in days. The rest of the table contains the flux density measurements of the pulsar (when detectable) and the total flux density (pulsed plus unpulsed) obtained at each of the four frequencies using the techniques described in the previous section.

3.1 Pulsed Emission

The pulsar fluxes are shown in the lower panel of Figure 2. Before periastron, the pulsar was detected at all frequencies at $\mathcal{T}-46$. At $\mathcal{T}-32$ the pulsar was scattered at 2.5 GHz and not detected at 1.4 GHz, at $\mathcal{T}-24$ scattering was evident at 4.8 GHz and the pulsar not detected at the two lower frequencies. However, at $\mathcal{T}-22$ the pulsar was again detected at 2.5 GHz but was scattered at that frequency two days later. At $\mathcal{T}-18$ the evidence for pulsed emission at any frequency is marginal although it cannot be ruled out. Following this date there is no further detection of pulsed emission until $\mathcal{T}+18$. Post-periastron, there is a clear detection at the two higher frequencies at $\mathcal{T}+18$ and shortly after the end of the ATCA observation the pulsar was also detected at Parkes at 1.3 GHz. Following this, the pulsar was detectable again at all frequencies.

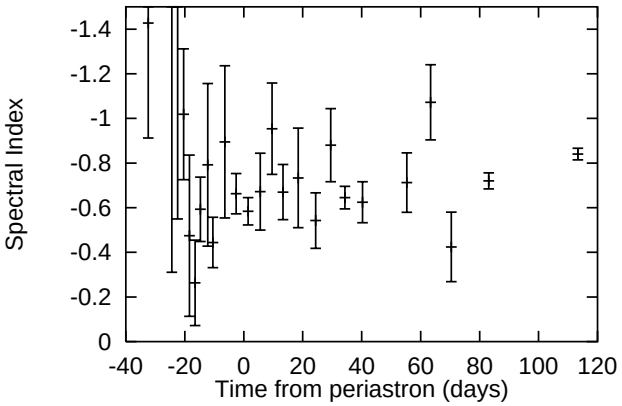

Figure 3. Spectral indices for the unpulsed emission.

It seems likely therefore that scattering dominates the detectability of the pulsar for ∼20 days leading up to $\mathcal{T}-16$. From this date until $\mathcal{T}+18$ the pulsar is behind the emission disc with respect to the observer and the pulsed emission is quenched by the high optical depth. The pulsar then appears to emerge from the disc rather abruptly; the scattering is marginal although optical depth effects are still visible at 1.4 GHz until $\mathcal{T}+25$. Unfortunately, the poor time resolution of our data precludes measurement of the scattering parameters.

In 1997 the pulsar was detected with the ATCA until $\mathcal{T}-21$ at all frequencies and at Parkes until $\mathcal{T}-18$. Post-periastron it was detected from $\mathcal{T}+16$ onwards. The effects of the wind on the pulsed emission therefore occurred earlier and lasted longer in 2000 than in 1997.

3.2 Unpulsed emission

The top panel of Figure 2 shows the light curve for the unpulsed emission. Unpulsed emission appears to be present at 1.4 GHz during the first observation at $\sim \mathcal{T}-46$ and remains roughly constant until $\sim \mathcal{T}-20$. The flux density then rapidly increases (to 40 mJy at 1.4 GHz) towards the first peak at $\sim \mathcal{T}-6$. A decrease with a similar slope follows, between $\sim \mathcal{T}-6$ and $\mathcal{T}+2$. The flux density plateaus (at $\sim$ 21 mJy at 1.4 GHz) at all frequencies between $\mathcal{T}+1$ and $\mathcal{T}+13$, and then rises again to a peak at $\sim \mathcal{T}+22$. The rise to the second peak is slower than the first, and the subsequent decay is rather shallow. $\mathcal{T}+70$ shows a sudden drop in the flux density, subsequently however the unpulsed emission remains clearly present at the two lower frequencies during our final observation at $\mathcal{T}+113$. This is similar to data taken in 1994 which shows unpulsed emission present at 0.84 GHz until at least $\mathcal{T}+132$ (Johnston et al. 1999). The data do show, however, that unpulsed emission is not present at 8.4 GHz from $\mathcal{T}+63$ onwards and has also vanished at 4.8 GHz by $\mathcal{T}+113$.

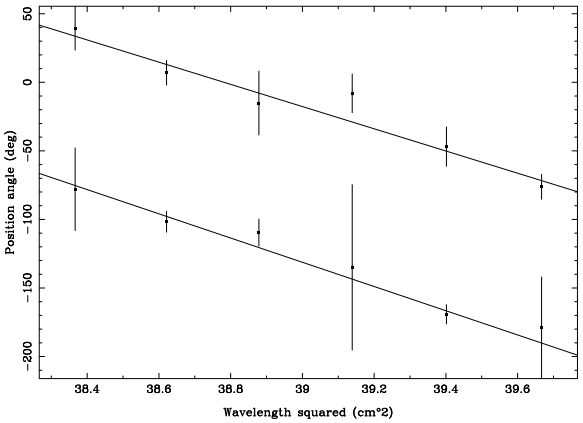

Figure 4. Position angle versus λ^2 across the 4.8 GHz band on September 1 for the first (top) and second (bottom) components. The position angle separation between the components is near 110°, as expected. The straight lines show the fit to the data from which the RM can be derived.

3.3 Spectral indices

The flux density at a frequency ν is given by $S_\nu = C\nu^\alpha$ where α denotes the spectral index. We measure the spectral index for the non-pulsed emission using flux densities obtained at each of our four observing frequencies. We apply a simple linear fit to log S - log ν space and assume symmetrical errors in log S. The spectral indices are shown in Figure 3 and are consistent with a value of ~ -0.7 throughout. There is no evidence for optical depths effects, at least at frequencies above 1 GHz. This is similar to the behaviour in 1997 (Johnston et al. 1999).

We do not attempt to measure the spectral index of the pulsed emission. At 8.4 GHz, diffractive scintillation significantly affects the observed flux density. The scintillation bandwidth of ∼70 MHz and timescale of ∼10 min (McClure-Griffiths et al. 1997) match well with our observing bandwidth of ∼120 MHz and time of 20 min. Furthermore, there is clear evidence for optical depth effects at low frequency post-periastron. In particular, the flux density at 1.4 GHz appears to increase steadily from $\mathcal{T}+21$ to $\mathcal{T}+70$ whereas this is not the case at the two higher frequencies.

3.4 Polarisation and Dispersion Measure

The circular polarisation was obtained for each pulse component for each observation, with errors of order $\sim 5\%$ at the lower frequencies, and $\sim 10\%$ at the higher frequencies due to the higher system temperature and lower flux density at these frequencies. The data are consistent with a mean value in the range -6% to -10% for the first component, and between -28% and -30% for the second component for all frequencies, in agreement with observations made at Parkes (see also Fig 1). We are thus confident that our polarisation calibration and analysis techniques are correct.

We attempted to obtain RMs and DMs for all days when the pulsar was not eclipsed using the techniques described in Section 2. These are presented in Table 3. The RM values are weighted averages of each of the two pulse components. In all cases the RMs agreed within the errors. Note that in general for RMs $\lesssim$2000 rad m^{-2}, only the two lower frequencies will show a significant position angle change across the bandpass whereas for RMs $\gtrsim$5000 rad m^{-2} depolarisation will occur even across a single channel at 2.4 GHz.

Prior to periastron, $\mathcal{T}-46$ was the only occasion on which we were able to derive an RM from the pulsar. At 8.4 GHz, the value we derived is -15200 rad m^{-2}. As detailed in Section 2, the data are obtained in 20 min sections at the high frequencies followed by 20 min at the low frequencies. We therefore divided the 4.8 GHz data into four 20 min sections and derived the RMs independently. Figure 4 shows the position angles obtained across the 4.8 GHz band during the third observation on $\mathcal{T}-46$ (Sep 1) and the fitted slope. The RMs measured on this date are extremely high, the highest astrophysical RM measurement as far as we are aware. There is also marginal evidence for a varying RM throughout the observing period. We presume that the RM increased even further after this date ensuring depolarisation even at 8.4 GHz on Sep 15 ($\mathcal{T}-32$).

On $\mathcal{T}+18$ there is a marginal detection of the pulsar but no RM or DM can be obtained. On $\mathcal{T}+21$, only the two lowest frequencies were observed but polarisation is clearly seen at 2.4 GHz and we derive an RM of -5100 rad m^{-2}. On $\mathcal{T}+24$, the RM has dropped significantly, however, on $\mathcal{T}+29$ the RM is large and positive but can only be detected in the first 20 min integration at 4.8 GHz as detailed in the table. We note that this is the only positive value of RM obtained. A similar result was obtained during the 1994 periastron, where the RMs were consistently negative both before and after periastron. Finally, as late as $\mathcal{T}+63$ the pulsar appears depolarised at all but 8.4 GHz. During the first 20 min observation at 4.8 GHz we measured an RM of -7700 rad m^{-2}.

There is only marginal evidence for a variable DM with epoch, with the errors quoted in the table being much larger than the typical 0.2 – 0.4 cm^{-3}pc obtained using pulsar timing (Johnston et al. 1996). The mean of the values quoted is 146.8 cm^{-3}pc, almost exactly the result obtained from timing. We note that these results are consistent with the values obtained during the 1994 and 1997 periastra. In 1994, the ΔDM (i.e. the DM with respect to 146.8 cm^{-3}pc) was 3.7 cm^{-3}pc by $\mathcal{T}-28$ and no change in DM was seen post-periastron (Johnston et al. 1996). In 1997, the ΔDM was 1.5 cm^{-3}pc on $\mathcal{T}-48$ and 4 cm^{-3}pc on $\mathcal{T}-42$. An upper limit of 0.2 cm^{-3}pc to the ΔDM was obtained post-periastron (Johnston et al. 2001).

From the current data we therefore set an upper limit to ΔDM on $\mathcal{T}-46$ of 3.0 cm^{-3}pc and on $\mathcal{T}+29$ of 5.8 cm^{-3}pc (i.e. twice the error bars), although from the above discussion the ΔDM is likely to be much smaller on the latter date. The magnetic field parallel to the line of sight, $B_\parallel$ in μG, can be obtained with knowledge of the RM and ΔDM by

$$B_\parallel = 1.232 \frac{\mathrm{RM}}{\Delta\mathrm{DM}} \quad (5)$$

where RM and ΔDM are in conventional units. The lower limits of $B_\parallel$ on $\mathcal{T}-46$ (Sep 1) and $\mathcal{T}+29$ (Nov 15) are therefore 6.2 mG and 1.6 mG respectively.

Date	($+\mathcal{T}$)	Time UT	Rotation Measure (rad m^{-2}) 1384 MHz	2496 MHz	4800 MHz	8640 MHz	DM cm^{-3}pc
Sep 01	−46.4	00:45 – 01:05			−14800±1800		
		01:35 – 01:55			−6900±5000		
		02:25 – 02:45			−12500±1400		
		00:45 – 03:45				−15200±3500	148.7±1.5
Nov 07	21.3			−5100±360			
Nov 10	24.4		−450±60	−460±180			145.7±2.9
Nov 15	29.5	22:30 – 22:50			+7700±2100		148.9±2.9
Nov 20	34.3		−360±5	−350±120			144.1±3.7
Nov 26	40.3		−675±30	−750±100			144.4±2.3
Dec 11	55.3		−101±9	−75±30			148.4±1.6
Dec 19	63.4	21:05 – 21:30			−7700±2400		146.9±2.4
Dec 26	70.4	19:25 – 21:00	−94±14				
		21:00 – 23:30	−50±7	−102±50			147.8±2.0
Jan 08	83.1		−49±9	−24±35			147.6±1.6
Feb 07	113.3		13±11	130±80			145.1±2.5

Table 3. RM and DM of the pulsar at various epochs averaged over the two pulse components. The errors are 1 σ. Where no time range is given the entire observation was used.

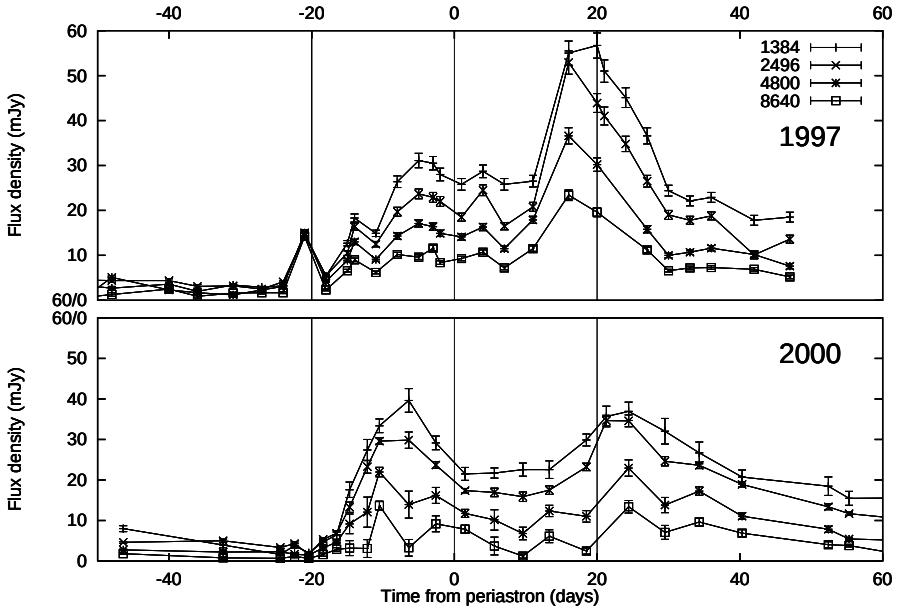

Figure 5. Light curves from the 1997 and 2000 data (pulsed and unpulsed flux combined) on the same scale. The vertical lines at $\mathcal{T} \pm 20$ delineate the approximate eclipse of the pulsar.

4 DISCUSSION

A comparison of the light curves of 1997 and 2000 appears in Figure 5. The same basic behaviour is seen for both sets of observations. There is a clear peak before and after periastron with a plateau in between. The transient emission also persists until late times in both. However, the initial 'blip' in the light curve seen at $\mathcal{T} - 21$ in 1997 was not repeated in 2000. Johnston et al. (2001) identified this as a transient event possibly associated with the pulsar 'splashing' into the disc. Also, in 2000, the first peak occurs earlier and the second peak later than in 1997. This is consistent with the longer lasting eclipse of the pulsed emission. The other striking feature is that the second peak is significantly lower in 2000 than in 1997. In broad terms, therefore, the model proposed after the 1997 periastron is repeated again. The pulsar enters the disc of the Be star near $\mathcal{T} - 20$, electrons are accelerated in the interface between the pulsar wind and the disc material. This occurs over the few days that the pulsar takes to cross the disc. When the pulsar leaves the disc, the wind bubble remains behind and decays through synchrotron losses. During the second crossing of the disc near $\mathcal{T} + 20$ the same process happens again causing the second peak seen in the light curve.

In Fig 6 we again show the light curve at 1.4 GHz. The decay of the second peak is clearly not linear, but follows a more power-law like behaviour. This is the expected form of the flux density for adiabatic expansion of a synchrotron bubble. We can write the synchrotron flux density, S_ν, from an expanding bubble as

$$S_\nu \propto L^{2\alpha-2}\ B^{1-\alpha}\ \nu^{\alpha} \qquad (6)$$

where L is the radius of the bubble, B is the magnetic field,

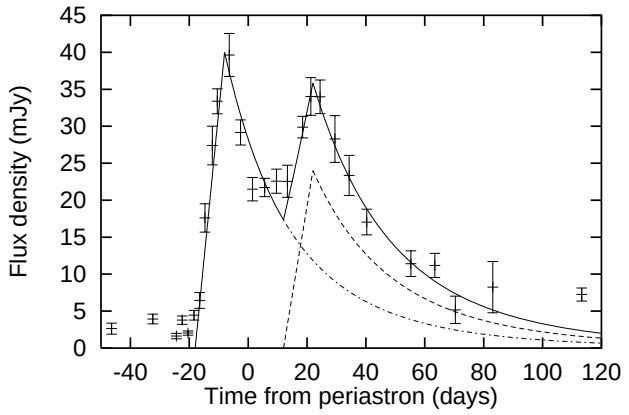

Figure 6. Flux density of the unpulsed emission at 1.4 GHz. Superposed is the solution to the model described in the text. The model includes a rise time of 10 days and adiabatic expansion for each of the synchrotron bubbles created in the disc crossings. The dashed lines indicate the light curve for each bubble individually. The solid line is the sum of both light curves.

and ν and α are the frequency and spectral index respectively. Imagine the synchrotron bubble is formed at an initial distance R_0 from the Be star and with an initial radius L_0. We then assume that the bubble moves outwards in the disc of the Be star with a velocity V. Hence

$$R(t) = R_0 \ + \ V\,(t - t_0) \tag{7}$$

where t_0 is the start time of the adiabatic phase. The change in R is evidently $R(t)/R_0$. We assume that the density in the disc follows a power-law with distance from the star i.e. $\rho(R) = CR^{-n}$. It then follows that

$$\frac{\rho(t)}{\rho_0} = \left(\frac{R_0 \ + \ V\,(t - t_0)}{R_0} \right)^{-n} \tag{8}$$

As the size of the bubble is dictated by the ram pressure between the pulsar wind and the disc material then $L \propto \rho^{-1/2}$ and so

$$\frac{L}{L_0} = \left(\frac{R_0 \ + \ V\,(t - t_0)}{R_0} \right)^{n/2} \tag{9}$$

The magnetic field in the disc is radial at the distances relevant here (Melatos, Johnston & Melrose 1995) and so

$$\frac{B}{B_0} = \left(\frac{R_0 \ + \ V\,(t - t_0)}{R_0} \right)^{-1} \tag{10}$$

Substituting these last two equations into equation 6 above we finally obtain

$$S_\nu = S_0 \ \left(\frac{R_0 \ + \ V\,(t - t_0)}{R_0} \right)^{(\alpha-1)(1+n)} \ \nu^\alpha \tag{11}$$

We model the data as follows. We set $\alpha = -0.6$ from the observations and assume $n = 3$ (Waters et al. 1991). We assume that t_0 for the first encounter is $\mathcal{T} - 8$ and for the second is $\mathcal{T} + 21$. The distance from the Be star at these epochs are 34 R_* and 42 R_* respectively. The interaction between the pulsar wind and the Be star's disc continues for $\sim$10 days. During this time electrons are injected continuously and a linear rise in the flux density provides a good fit to the data. We then fit the entire data set using the functional form of equation 11 and with S_0 for both encounters and V as free parameters. The solution yields S_0 of 40 and 24 mJy respectively (at 1.4 GHz) and $V = 12$ km s^{-1} and this solution is shown in Fig 6. The ratio of the peak fluxes is in agreement with the relative distance from the Be star of the two start epochs. We note that although the fit is generally good it falls well below the measured flux density of the last data point at $\mathcal{T} + 113$. It is also evident that some unpulsed emission is present as early as $\mathcal{T} - 46$ at least at low frequencies. There therefore appears to be some low-level emission unrelated to the disc crossings. This emission could arise with the interaction between the pulsar wind and dense clumps in the (more tenuous) Be star wind. We repeated the fitting process but in addition we had a constant offset of 4 mJy throughout the entire observing period to represent the low-level emission. This naturally provides an improved fit to both very early and very late times. However, V is largely unchanged at 15 km s^{-1}.

There is a strong similarity between the system under discussion here and the LSI+61°303 binary. There, an unseen neutron star orbits a Be star in a highly eccentric orbit with a period of only 26 days. Radio outbursts show a steep rise followed by a power-law like decay. Paredes et al. (1991), in a more complete treatment, modelled the radio light curve of LSI+61°303 in a similar fashion to undertaken here - after a prolonged period of particle injection, they allowed the resultant synchrotron bubble to expand adiabatically. In their case, the light curve decays after only $\sim$10 days, and they derive an expansion velocity of 400 km s^{-1}. In our case, the light curve decays on a much longer timescale which naturally implies a much lower expansion velocity. A velocity of only 12 km s^{-1} is surprisingly low for the outflow of disk material at this distance from the Be star. Waters et al. (1987) show that the velocity is likely to be $\sim$100 km s^{-1} and indeed our optical observations of this star indicate a velocity of $\sim$80 km s^{-1} at 20 R_*. It is not clear, therefore, why our derived velocity is so low.

Synchrotron loss times, set by the magnetic field in the bubble, are also relevant but on a longer timescale than the adiabatic losses. As the synchrotron bubble evolves, the break frequency in the emission spectrum moves to lower frequencies. Once the break frequency becomes lower than the observing frequency, the flux density at that frequency should decline rapidly. The time, t_b, in days, at which the break frequency equals the observing frequency can be approximated as

$$t_b \approx 315 \ B^{-3/2} \nu^{-1/2} \tag{12}$$

where B is the magnetic field strength in Gauss and ν is in GHz. Given that no further injection of electrons occurs after $\mathcal{T} + 22$ and that the emission at 4.8 GHz appears to have decayed by $\mathcal{T} + 90$ we can therefore estimate the decay of the emission at 8.4, 2.5, 1.4 and 0.84 GHz should occur 73, 118, 150 and 185 days after periastron respectively. This is consistent with the lack of emission at 8.4 GHz from $\mathcal{T} + 63$ onwards and the detection of unpulsed emission at 1.4 and 0.8 GHz at least as late as $\mathcal{T} + 113$ and $\mathcal{T} + 132$. Using Equation 12, the magnetic field in the disc where the synchrotron bubble is created is $\sim$1.6 G. This is consistent with the result obtained by Ball et al. (1999). Note that, as expected, this value of the magnetic field in the disc significantly higher than the value we measured for the wind of the Be star.

5 CONCLUSIONS

A series of observations of the 2000 periastron of the PSR B1259−63/SS2883 system were made at the ATCA at four frequencies. The pulsar binning mode available with the ATCA correlator meant that pulsed and unpulsed emission could be separated and we therefore obtained light curves for the pulsar and unpulsed emission independently. We were also able to obtain RMs and DMs for the pulsar.

The main features in the light curve from the 2000 periastron are similar to the 1997 periastron, providing confirmation of our earlier model. It does appear, however, that the pulsar eclipse lasted longer and the unpulsed emission began and finished later in 2000 than in 1997. This indicates that the disc has become larger and/or denser in 3.5 yr. As we obtained more data at late times than in the previous periastron encounters, we found that adiabatic decay of the synchrotron bubble provided the best fit to the data. The expansion rate of the bubble, $\sim$12 km s^{-1}, is significantly lower than expected but the magnetic field value of 1.6 G consistent with measurements in other Be stars.

In addition, at $\mathcal{T} - 46$ the pulsar had the highest measured astrophysical RM of -14800 ± 1800 rad m^{-2} implying a magnetic field of at least 6 mG in the Be star wind.

ACKNOWLEDGEMENTS

The Australia Telescope is funded by the Commonwealth of Australia for operation as a National Facility managed by the CSIRO. We thank A. Karastergiou and B. Koribalski for help with the observing and A. Melatos for useful discussions.

REFERENCES

Ball L. T., Melatos A., Johnston S., Skjaeraasen O., 1999, ApJ, 514, L39
Johnston S., Lyne A. G., Manchester R. N., Kniffen D. A., D'Amico N., Lim J., Ashworth M., 1992a, MNRAS, 255, 401
Johnston S., Manchester R. N., Lyne A. G., Bailes M., Kaspi V. M., Qiao G., D'Amico N., 1992b, ApJ, 387, L37
Johnston S., Manchester R. N., Lyne A. G., Nicastro L., Spyromilio J., 1994, MNRAS, 268, 430
Johnston S., Manchester R. N., Lyne A. G., D'Amico N., Bailes M., Gaensler B. M., Nicastro L., 1996, MNRAS, 279, 1026
Johnston S., Manchester R. N., McConnell D., Campbell-Wilson D., 1999, MNRAS, 302, 277
Johnston S., Wex N., Nicastro L., Manchester R. N., Lyne A. G., 2001, MNRAS, 326, 643
Manchester R. N., Johnston S., 1995, ApJ, 441, L65
Manchester R. N., Taylor J. H., 1977, Pulsars. Freeman, San Francisco
McClure-Griffiths N., Johnston S., Stinebring D., Nicastro L., 1997, ApJ, 492, L49
Melatos A., Johnston S., Melrose D. B., 1995, MNRAS, 275, 381
Paredes J. M., Marti J., Estalella R., Sarrate J., 1991, AA, 248, 124
Sault R. J., Killeen N. E. B., 1998, The Miriad User's Guide. Australia Telescope National Facility, Sydney, (http://www.atnf.csiro.au/computing/software/miriad/)
Taylor J. H., Cordes J. M., 1993, ApJ, 411, 674
Waters L. B. F. M., Coté J., Lamers H. J. G. L. M., 1987, AA, 185, 206
Waters L. B. F. M., van der Veen W. E. C. J., Taylor A. R., Marlborough J. M., Dougherty S. M., 1991, AA, 244, 120
Wex N., Johnston S., Manchester R. N., Lyne A. G., Stappers B. W., Bailes M., 1998, MNRAS, 298, 997